Pharmaceutical Research (2024) 41:501–512
https://doi.org/10.1007/s11095-024-03671-9

ORIGINAL RESEARCH ARTICLE

Characterization of mRNA Lipid Nanoparticles by Electron Density Mapping Reconstruction: X-ray Scattering with Density from Solution Scattering (DENSS) Algorithm

Huy M. Dao[1] · Khaled AboulFotouh[1] · Aasim Faheem Hussain[2] · Alexander E. Marras[2,3,4] · Keith P. Johnston[5] · Zhengrong Cui[1] · Robert O. Williams III[1]

Received: 27 September 2023 / Accepted: 28 January 2024 / Published online: 7 February 2024

Abstract

Purpose This study aimed to test the feasibility of using Small Angle X-ray Scattering (SAXS) coupled with Density from Solution Scattering (DENSS) algorithm to characterize the internal architecture of messenger RNA-containing lipid nanoparticles (mRNA-LNPs).

Methods The DENSS algorithm was employed to construct a three-dimensional model of average individual mRNA-LNP. The reconstructed models were cross validated with cryogenic transmission electron microscopy (cryo-TEM), and dynamic light scattering (DLS) to assess size, morphology, and internal structure.

Results Cryo-TEM and DLS complemented SAXS, revealed a core–shell mRNA-LNP structure with electron-rich mRNA-rich region at the core, surrounded by lipids. The reconstructed model, utilizing the DENSS algorithm, effectively distinguishes mRNA and lipids via electron density mapping. Notably, DENSS accurately models the morphology of the mRNA-LNPs as an ellipsoidal shape with a "bleb" architecture or a two-compartment structure with contrasting electron densities, corresponding to mRNA-filled and empty lipid compartments, respectively. Finally, subtle changes in the LNP structure after three freeze–thaw cycles were detected by SAXS, demonstrating an increase in radius of gyration (Rg) associated with mRNA leakage.

Conclusion Analyzing SAXS profiles based on DENSS algorithm to yield a reconstructed electron density based three-dimensional model can be a useful physicochemical characterization method in the toolbox to study mRNA-LNPs and facilitate their development.

Keywords DENSS · mRNA-LNps · SAXS · solution scattering

✉ Zhengrong Cui
zhengrong.cui@austin.utexas.edu

✉ Robert O. Williams III
bill.williams@austin.utexas.edu

[1] Division of Molecular Pharmaceutics and Drug Delivery, College of Pharmacy, The University of Texas at Austin, Austin, TX 78712, USA

[2] Department of Biomedical Engineering, Cockrell School of Engineering, The University of Texas at Austin, Austin, TX, USA

[3] Materials Science and Engineering Graduate Program, Texas Materials Institute, The University of Texas at Austin, Austin, TX, USA

[4] Walker Department of Mechanical Engineering, The University of Texas at Austin, Austin, TX, USA

[5] McKetta Department of Chemical Engineering, The University of Texas at Austin, Austin, TX, USA

Introduction

Messenger RNA-containing lipid nanoparticles (mRNA-LNPs) are revolutionizing infectious disease prevention and have the potential to further transform healthcare in a range of therapeutic areas, including cancer, genetic disorders, infectious diseases, and autoimmune diseases [1]. While mRNA therapy and mRNA-LNPs have been in development for decades, they have recently gained increased attention after the approval of the mRNA-based COVID-19 vaccines, i.e., Pfizer/BioNTech's Comirnaty® and Moderna's Spikevax®.

A major challenge for development of these therapies is that, mRNA-LNPs are complex products that are inherently unstable. Sources of mRNA-LNP instability are both chemical (e.g., hydrolysis and oxidation of mRNA and lipids) and physical (e.g., LNP aggregation, RNA leakage) [2].

To ensure the development of effective and safe mRNA-LNP based therapeutic, a set of critical quality attributes (CQAs) must be established, including physicochemical characterization, *in vitro* cell transfection, and *in vivo* animal studies [2]. Physicochemical characterizations are usually performed during the early stages of research and development. In particular, the widely used set of techniques includes dynamic light scattering (DLS) to study particle size distribution (PSD), fluorescence-based binding assay to assess mRNA entrapment efficiency (EE), and capillary electrophoresis or HPLC to characterize mRNA integrity. A desirable set of physicochemical properties generally includes small PSD, low polydispersity index (PDI), high EE, and intact mRNA [2–4]. However, these methods are inherently scant on information as they only include a single data point to describe the mRNA-LNPs and thus are mostly utilized as quality control checkpoints. More specifically, despite having acceptable physicochemical properties, the mRNA-LNPs after being lyophilized and resuspended may demonstrate unacceptable *in vivo* transfection efficiency [4]. Furthermore, while the knowledge acquired via experimentation about the effect of lipid composition on mRNA-LNP stability and transfection efficiency is useful, the fundamental reasons underlining the trends and patterns observed from the studies and statistical analyses remain unknown without further understanding the molecular architecture of the various mRNA-LNPs and molecular interactions within them. This information can be obtained via several advanced methods such as NMR, cryo-EM, or X-ray scattering [5].

Small Angle X-ray Scattering (SAXS) has been employed to study mRNA-LNPs, aiming to enhance our understanding about their size and shape. However, while the information obtained from SAXS is useful in the detection of lamellar spacing and lipid structure [6], it does not provide detailed information about the localization of the mRNA and comprehensive architecture of the LNPs. Hetero-density particulate systems' (i.e., viruses) internal structure can be resolved by SAXS via contrast variation, however this is a time consuming and labor intensive procedure [7]. In light of this limitation, the Density from Solution Scattering (DENSS) algorithm, initially introduced by Thomas D. Grant (2018), enables the reconstruction of both 3D shape and electron density of the internal structure of studied objects through solution scattering SAXS profiles [8, 9]. Through the SAXS data, along with other conventional data that can be derived experimentally (i.e., size, shape, radius of gyration (Rg)), it becomes feasible to compute electron density profile of particles or macromolecules, reflecting spatial distribution of electrons within the entity.

Although DENSS has been used in various studies, its application has primarily been confined to the protein domains. Notably the DENSS algorithm has been employed to generate protein ensembles, subsequently aligned with crystal structure data across multiple instances, such as calmodulin upon interaction with antagonist [10], importin α1/β [11], phage E217 terminase E217 [12] pre-incision protein complex [13], the dumbbell-shaped Suv3 helicase and PNPase complex [14], and MicroRNA cluster [15]. Throughout these cases, DENSS was used in a manner similar to *ab initio* dummy atom modeling, to construct protein ensembles for further fitting with crystal structure obtained via other methods [16].

By capitalizing on its ability to construct models without the assumption of homogenous electron density as in conventional *ab initio* modeling, DENSS has been demonstrated as a potent algorithm for small angle scattering data processing. In a study involving d54- 1,2-ditetradecanoyl-sn-glycero-3-phosphocholine (DMPC) phospholipid nanodiscs, DENSS reconstructions showed a higher neutron scattering density in the center, matching the deuterated acyl chain of DMPC [17]. In the case of C-undecylcalix[4]resorcinarene self-assembled into hexameric capsule-like structures, the resultant electron density map exhibited a spherical particle with a hollow core where density in the core is similar to the toluene solvent. This structure also aligned with the structures obtained by the conventional dummy atom modeling DAMMIN program [18]. In the case of silica nanoparticles self-assembled into ring-like nanostructures in the presence of an amphiphilic block co-polymer, as confirmed by cryo-TEM, DENSS has demonstrated its ability to correctly reconstruct the irregular hollow star-shape model [19]. Most importantly, the capability of an improved version of DENSS has been demonstrated to reproducibly reconstruct entities with distinct internal contrasts, including 2-layer onions, 3-layer onions, nanodiscs, and 2-layer cylinders [20]. It is noted that simulated annealing using a multiphase dummy atom model software MONSA, the current state-of-the-art in multi-phase reconstruction, [21] largely struggled to capture the phase morphologies from the same datasets [20].

As aforementioned, while SAXS has been used to characterize LNPs, including mRNA-LNPs, it was used in a limited fashion of detecting repeating structures such as multilamellar lipid layer(s) in the LNP structure [6, 22, 23]. In this study, we investigated whether SAXS can be used to provide additional information such as the particle size (instead of hydrodynamic size based on DLS), location of mRNA in mRNA-LNP, presence of blebs in mRNA-LNP population, as well as change in mRNA-LNPs after being subjected to freezing stress. We hypothesized that the spatial arrangement of mRNA within the lipid core of the LNPs, and the overall architecture of LNPs can be elucidated through 3D reconstruction using DENSS. The rationale underlying this proposition rests upon the sufficient difference in scattering length density (SLD), a reflection of the combined (a) physical density and (b) intrinsic scattering power of the molecules, between mRNA and phospholipids. This difference

allows for the differentiation between mRNA and phospholipids via DENSS. In this study, we investigated Moderna's bivalent COVID-19 vaccine and an in-house polyadenylic acid [poly(A)] loaded LNP as the model mRNA-LNPs. The SAXS profiles of the samples, including the synchrotron SAXS profiles of the COVID-19 vaccine, were collected, analyzed, and subsequently the DENSS algorithm was employed to construct a 3D model of the average individual mRNA-LNP. This model was then cross-referenced to compare to other characterization techniques including cryo-TEM and DLS to verify model accuracy.

Materials and Methods

Materials

Moderna's COVID-19 bivalent vaccine in-date, lot number 030G22B, were kindly donated by the 38th Street Pharmacy, Austin, TX. Each 0.5 mL dose of the vaccine contains 100 µg nucleoside-modified mRNA encoding the pre-fusion stabilized spike glycoprotein (S) of the SARS-CoV-2 virus. Each dose contains a total lipid content of 1.93 mg (3.86 mg/mL) (SM-102, polyethylene glycol (PEG) 2000 dimyristoyl glycerol (DMG), cholesterol, and 1,2-distearoyl-sn-glycero-3-phosphocholine (DSPC)). Other excipients in each dose include 0.31 mg tromethamine, 1.18 mg tromethamine hydrochloride, 0.043 mg acetic acid, 0.12 mg sodium acetate, and 43.5 mg sucrose.

Quanit-iT™ RiboGreen® RNA Reagent and Kit (Invitrogen) and Vivaspin® 4 Turbo centrifugal concentrator with 30 kDa membrane MWCO were from ThermoFisher Scientific Inc. (Waltham, MA). Glass number 50 capillaries for SAXS, with outer diameter of 0.1 mm were from Hampton Research Aliso Viejo, CA, USA.

The (6Z,9Z,28Z,31Z)-heptatriacont-6,9,28,31-tetraene-19-yl 4-(dimethylamino) butanoate (DLin-MC3-DMA) was from MedChem Express (Monmouth Junction, NJ). DSPC and 1,2-distearoyl-sn-glycero-3-phosphoethanolamine-N-[amino(polyethylene glycol)-2000] ammonium salt (PEG_{2000}-DSPE, MW ≈ 2790) were from Avanti Polar Lipids (Alabaster, AL). Cholesterol was from Sigma-Aldrich (St. Louis, MO). Poly(A) (MW 700–3,500 KDa) was from Roche Diagnostics GmbH (Mannheim, Germany).

Poly(A)-LNPs Synthesis

Poly(A)-LNPs were synthesized as reported previously [24]. In brief, lipid components were dissolved in ethanol with the following molar ratio DLin-MC3-DMA: DSPC: Cholesterol: PEG_{2000}-DSPE (40:5:38.5:0.5) corresponding to lipid molar percentage (47.62: 5.95: 45.3:0.60). Ethanolic solution of lipids and the aqueous solution of poly(A) in RNAse-free citrate buffer (pH 3, 25 mM) at a ratio of 1:3 v/v, respectively, were rapidly mixed by pipetting. The final N/P ratio of the formulation was 3:1. Following mixing, the poly(A)-LNPs were dialyzed overnight against 250 × sample volume of RNAse-free water using a SpectraPro Float-A-Lyzer G2 Dialysis Device with a molecular weight cutoff of 100 kDa (Spectrum Laboratories, Inc., Rancho Dominguez, CA). The dialysis medium was exchanged twice. Then, the poly(A)-LNPs were diluted with D-(+)-trehalose dihydrate (TCI Co., LTD, Tokyo, Japan) in RNAse-free water (Thermo Fisher Scientific) at 5% w/v concentration. The resultant mRNA-LNPs have 1.6 mg/mL total lipid content and 165 µg/mL of poly(A). Blank RNA-free LNP samples were prepared in the exact manner as the poly(A)-LNPs without poly(A).

Measurements of Size and Zeta Potential

A Zetasizer ZS (Malvern Analytical, UK) was used for the DLS measurements to monitor the hydrodynamic size of the mRNA-LNPs. The lipid suspension was loaded into a semi-micro disposable plastic cuvette at a 100 times dilution (38.6 µg total lipid /mL) with 0.01 M pH 7.4 PBS and sealed with parafilm. DLS was performed on diluted samples at 25°C with 173° scattering angle and the reported z-average diameter is a mean of three measurements. Subsequently, zeta potential was measured using dip-cell (Malvern Analytical, UK) by dipping into the same sample-containing cuvette.

Determination of mRNA Encapsulation Efficiency

The mRNA encapsulation efficiency was evaluated by low range Quant-iT® RiboGreen RNA reagent assay. Each LNP sample was diluted with Tris–EDTA (TE) buffer down to a mRNA concentration of 2–200 ng/µL. Aliquots of each LNP working solution were further diluted 1:1 in TE buffer (measuring unencapsulated mRNA) or 1:1 in TE buffer with 1% Triton-X100 (measuring total mRNA) in a 96-well plate. Samples were prepared in triplicate and 100 µL of 2000-fold diluted Quant-iT® RiboGreen RNA reagent was added to each sample. The fluorescence intensity was measured using a plate reader at excitation and emission wavelengths of 480 and 520 nm, respectively.

Small Angle X-ray Scattering (SAXS) and Data Analysis

SAXS measurements were carried out using a SAXSLabs GANESHA instrument with a CuKα wavelength (1.5406 Å) and a beam size of 0.2 mm. The mRNA-LNPs suspension was concentrated by centrifugation using the Vivaspin® 4 Turbo device (30,000 Da MWCO) at 3,000 rpm in the Sorval RTH-750 rotor to achieve the appropriate concentration (3.86 mg/mL to 38.6 mg/mL total lipid concentration for

Moderna's COVID-19 vaccine; and 16 mg/mL total lipid concentration for poly(A)-LNP). The increase in sample concentration was designed to lower collection time and compensate for the low brilliance of the CuKα x-ray compared to synchrotron beamline. The buffer collected at the bottom of the centrifugal tube was used as the blanking solution. The resulting concentrated LNPs suspension was loaded into a glass capillary with a diameter of 0.9 mm and a wall thickness of 0.01 mm. The capillary was sealed with glue to prevent solvent evaporation under vacuum. Each sample, with a particle concentration of approximately 10–30 mg/mL, was measured for 60, 30, and 5 min at 25°C for extra-small-angle (ESAXS), small-angle (SAXS), and medium-angle X-ray scattering (MAXS), respectively. A background measurement of air/buffer in the same capillary was acquired using the same settings and subtracted from the sample measurements. Scattering intensity was recorded using a Pilatus 300K solid-state photon-counting detector, providing access to a q-range of 0.00497 to 0.4157 Å.$^{-1}$

The synchrotron SAXS was carried out at the SLAC National Accelerator Laboratory (Menlo Park, CA); at beam line 4–2, with a Pilatus3 X 1M detector with q range of 0.0034 to 0.33 Å^{-1}. A 20 µL samples was loaded into the flow cell from the 96-well plate by an automated liquid sample loader.

BioXTAS RAW 2.1.4 software [25] and GNOM package [26] were utilized to carry-out Guinier and pair distribution function p(r) analysis. The maximum linear dimension of the molecule, Dmax, is calibrated for goodness-of-fit by enforcing a smooth zeroing of P(Dmax). DENSS was used to calculate the *ab initio* electron density map directly from the GNOM output. Twenty reconstructions of electron density mapping were performed in slow mode using default parameters and subsequently averaged. Alignment of the reconstructions to the structure was achieved using the DENSS alignment function in BioXTAS RAW. The reconstructions were visualized using PyMOL 2.5.2 Molecular Graphics System (Schrödinger, LLC. New York, NY) with five contour levels of the density map and their respective colors: 15σ (red), 10σ (green), 5σ (cyan), 2.5σ (blue), and 1σ (violet). The sigma (σ) level denotes the standard deviation above the average electron density value of the reconstructed LNP model. A five-sigma level (5σ) contour will envelope a region that has electron density values greater than five sigmas over the average value.

Cryogenic Transmission Electron Microscopy

The structures of the Moderna's COVID-19 bivalent vaccine and the poly(A)-LNPs were examined using Cryo-TEM. The total lipid concentration of the samples was 3.96 mg/mL. In the grid preparation, Au-Flat gold film grids (Protochips, Albuquerque, NM) and lacey carbon film grids (Electron Microscopy Sciences, Hatfield, PA) were plasma-cleaned for 1 min in a Pelco easiGlow glow discharge system (Ted Pella Inc., Redding, CA). LNP (4 µL) were deposited on the grid mesh using a Vitrobot Mark IV system (Thermo Scientific) in the 100% humidity chamber for 3.5 s with a force of -4 at 25°C, and then the excess liquid was blotted away using grade 595 vitrobot filter paper (Ted Pella Inc.). The grids were subsequently immersed into liquid ethane. Frozen grids were transferred and imaged on a Glacios operated at 200 kV and equipped with a Falcon 4 direct detector (Thermo Fisher Scientific). Captured movies were collected and analyzed using SerialEM at a magnification of 150,000 × with an exposure time of 13.2 s, at a total dose of 50 e−/Å2, corresponding to a calibrated pixel size of 0.94 Å/pixel. The resultant MRC formatted images were processed by IMOD 4.11 software [27].

Results

Comparison Between Extra-Small, Small, and Medium Angle X-ray Scattering

The X-ray profiles of the Moderna COVID-19 bivalent vaccine samples were collected at three different angles, namely in the extra-small (ESAXS), small (SAXS), and medium (MAXS) modes. The scattering vectors with the lowest q values, along with their respective d-spacing, for these three scanning angles were: 0.002458 Å^{-1} (255.6 nm) for ESAXS, 0.00421 Å^{-1} (149.2 nm) for SAXS, and 0.0113 Å^{-1} (5.56 nm) for MAXS. Given that the hydrodynamic diameter (z-average) of the mRNA-LNPs in Moderna COVID-19 vaccine was approximately 145 nm, as measured by DLS (Table I) ESAXS and SAXS are appropriate for subsequent analyses because they provide more information about the size and shape of the LNPs, as the smallest q value corresponding to the size of the LNPs. Also it should be mentioned that the physical size of the LNP, excluding electrical double layer and layer of solvent that diffuse along the LNP, could be smaller than 145 nm. While ESAXS did provide six additional data points, extending the q to 0.002458 Å^{-1} (255 nm), it significantly increased the run time from 1800 to 3600 s to gather sufficient scattered data, as compared to SAXS. It is worth noting that the lab-scale GANESHA ESAXS lowest q is even lower than synchrotron SAXS at 0.00358 Å^{-1} (Fig. 1A). Thus ESAXS is operating at the equipment limit and yield unreliable data as demonstrated by the level of noise and different reconstructed model, as compared to SAXS and synchrotron SAXS (Fig. 1A). Furthermore, the runtime extension also increased the risk of damaging due to prolonged X-ray exposure. The data quality also deteriorated quickly as the q values were increased, causing notable noise in the 100 to 10 nm region. On the

Table I Pair distribution Function Analysis Data of mRNA-LNPs in Moderna's COVID-19 Vaccine. Data from ESAXS, SAXS, Merged (i.e., ESAXS/SAXS/MAXS), and Synchrotron are Shown. The mRNA-LNP Diameter from DLS (Dh), Polydispersity Index (PDI), mRNA Encapsulation Efficiency (EE), and Zeta Potential Values are Also Shown

	ESAXS	SAXS	Merge	Synchrotron		DLS/EE
Rg (Å)	268 ± 32	265 ± 7	265 ± 3	286 ± 1		
Dmax (Å)	852	846	800	850	Dh (Å)	1,441 ± 24
I(0)	65 ± 11	60.7 ± 2	67.9 ± 2	7.4 ± 0.08	PDI	0.188 ± 0.010
$\chi 2$	1.2363	0.9514	1.0947	1.1747	EE (%)	95.3 ± 2.1
Total Estimate	0.7995	0.7664	0.5546	0.8343	Zeta potential (mV)	-2.1 ± 0.1

Analysis cannot be performed on MAXS due to the inherent high q-value cut off

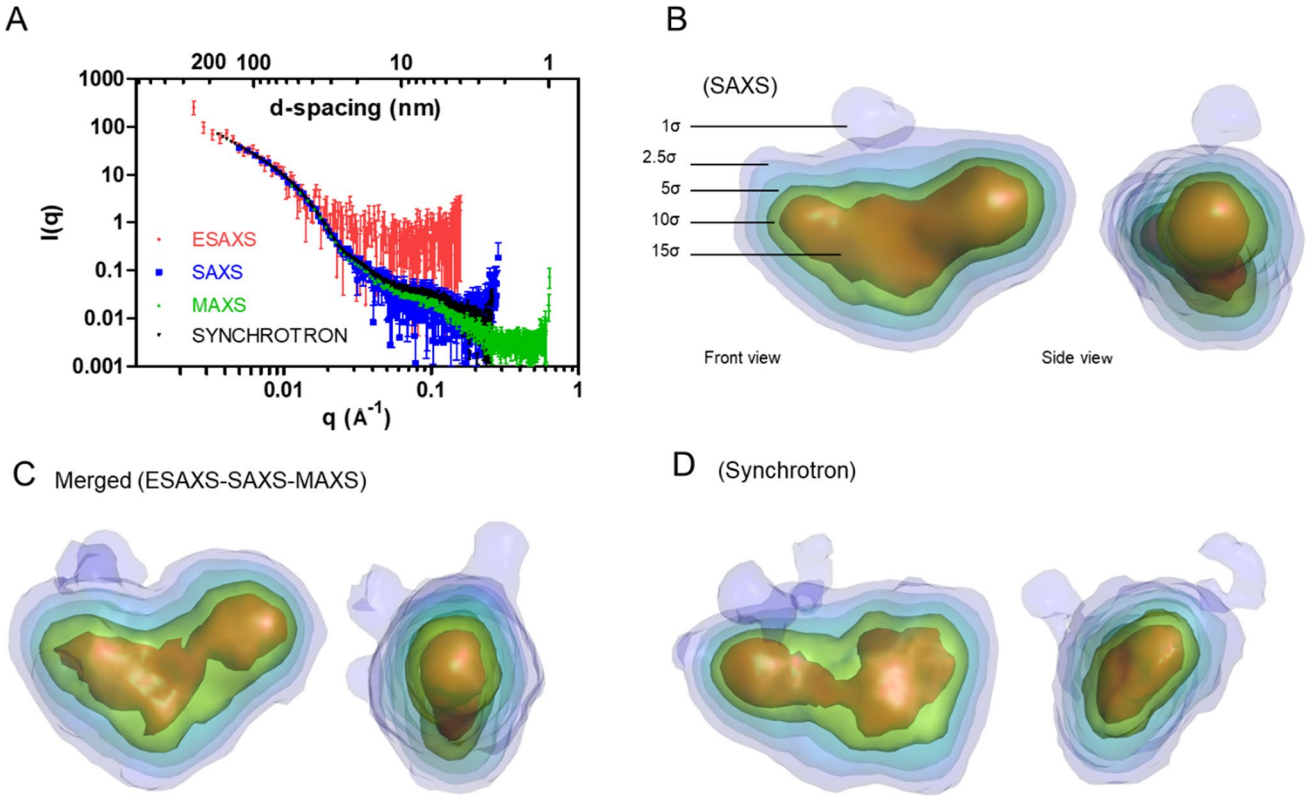

Fig. 1 (**A**) Lab-scale ESAXS, SAXS, MAXS, and synchrotron SAXS profiles of Moderna's COVID-19 bivalent vaccine, (**B**-**D**) reconstructed 3D models of the mRNA-LNPs by DENSS algorithm of SAXS, merged and synchrotron data showing front view (left), and side view (right). Reconstructions were visualized using PyMOL 2.5.2 with five contour levels of the density map with their respective color: 15σ (red), 10σ (green), 5σ (cyan), 2.5σ (blue), and 1σ (violet). Particles size not drawn to scale of the Dmax.

other end, MAXS proved insufficient for gleaning information about the size and shape of the mRNA-LNPs. It instead provided data about the internal structure. Overall, no discernible peak was observed in the higher q-region, suggesting an absence of significant repeating patterns or orderly structure such as multilamellar in the LNPs (Fig. 1A).

The repeatability of synchrotron SAXS data is demonstrated in Figure S1 showing identical curves over three separate sample loadings and runs. Furthermore, the merging of lab-scale ESAXS, SAXS, and MAXS data yields a single X-ray profile with lower noise level (Figure S1). The merged lab-scale X-ray scattering curve is similar to that of synchrotron SAXS.

The lab-scale and synchrotron X-ray scattering data were further analyzed using the GNOM package (an indirect transform program for small-angle scattering data processing) to fit the raw data producing a pair distribution function p(r) and the respective Rg and effective maximum particle dimension (Dmax) (Table I). The results showed that the calculated parameters are roughly similar, with Rg values ranging from 265 to 286 Å and Dmax from 800 to 852 Å. The results indicated that data yielded from lab-scale X-ray scattering is comparable to

that from synchrotron SAXS, and the yielded data are consistent using either merged or individual SAXS curve.

The average reconstruction models by DENSS are presented in Fig. 1B-D. These images represent the front and side views of an average individual mRNA-LNP in the liquid suspension. The final reconstruction was obtained by averaging 20 separate reconstruction attempts from the p(r) function. The models were color coded in five contours with hot-warm (red, green) colors denoting elevated electron density and cold colors (cyan, blue, violet) denoting lower electron density regions. As can be seen, the model showed an ellipsoidal shape with high electron density region in the core, which could be attributed to mRNA due to higher scattering length density compared to the phospholipids. The overall shapes of the reconstructed models are similar, suggesting the work flow and data processing to extract p(r) function and subsequently modelling by DENSS is consistent. As the data and reconstructed models from lab-scale SAXS and synchrotron SAXS are comparable, additional studies were done with lab-scale SAXS only.

SAXS Profiles of mRNA-LNPs at Different Lipid Concentrations

To confirm the accuracy of the analysis and reconstruction, the entire process was conducted using different mRNA-LNP concentrations, ranging from 1 to 10 times the original concentration at total lipid concentration of 3.86, 9.65, 19.3, and 38.6 mg/mL; and mRNA concentrations of 200, 500, 1000, and 2000 µg/mL, approximately; achieved through centrifugal filtration to increase the signal-to-noise ratio. At each concentration interval, a small volume of the liquid sample was set aside for DLS measurements to confirm that the centrifugation process did not modify the size and size distribution of the mRNA-LNPs.

The results demonstrated that varying concentrations of mRNA-LNPs generated similar SAXS profiles (Fig. 2A) and p(r) function (Fig. 2B). Similarly, mRNA-LNPs at different (lipid) concentrations also yielded comparable reconstructed models based on the DENSS algorithm Fig. 2C-F. These models highlighted several notable features of the

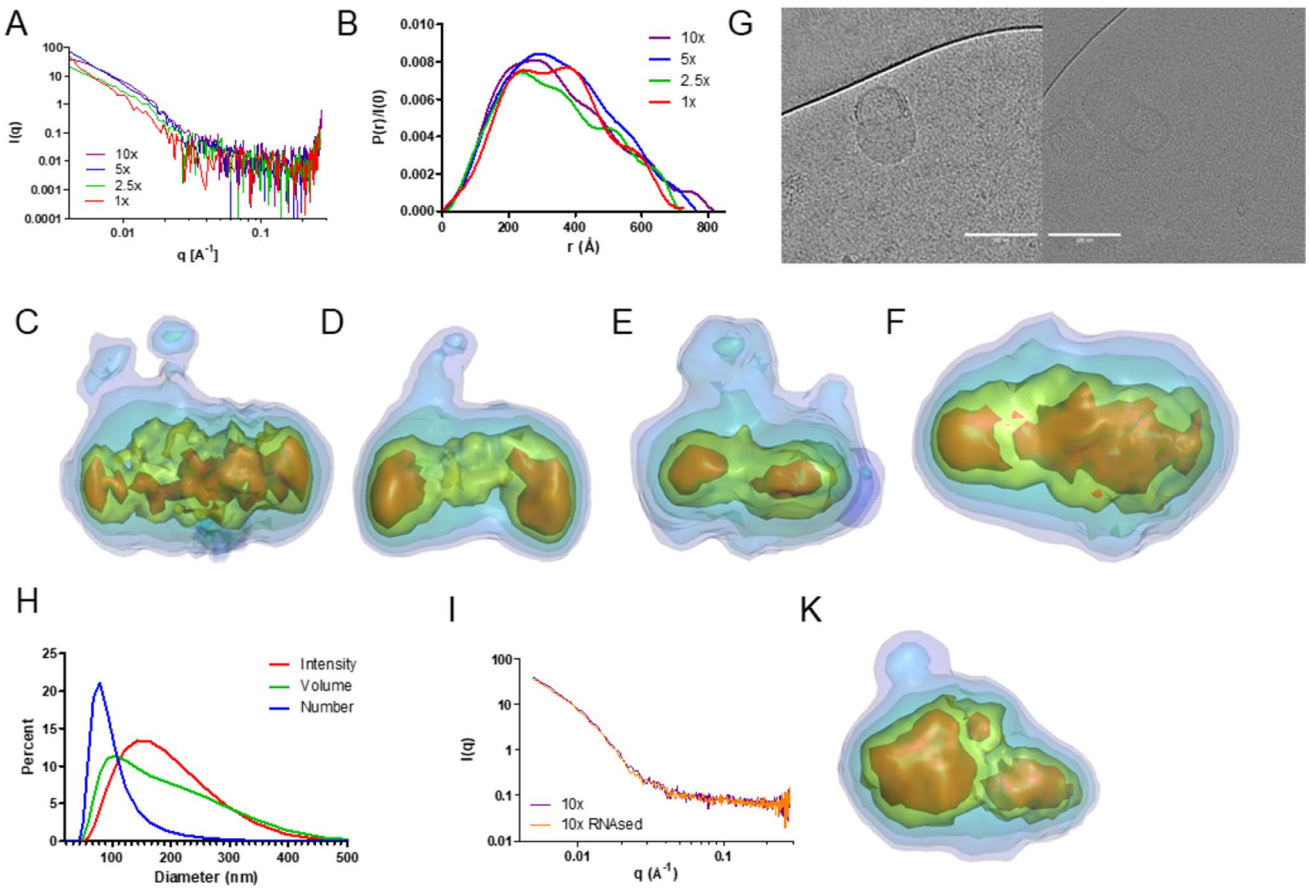

Fig. 2 (**A**) SAXS profiles and (**B**) normalized p(r) functions of Moderna COVID-19 vaccine at 1 to 10×concentration, (**C**-**F**) DENSS reconstructed models of mRNA-LNPs at 1 to 10×concentration (3.96 to 39.6 mg/mL total lipid content), (**G**) cryo-TEM image of the mRNA-LNPs, (**H**) particle size distribution of mRNA-LNPs based on intensity, volume, and number, (**I**-**K**) SAXS profiles and reconstructed models of mRNA-LNPs reference and RNAse spiked samples. Reconstructions were visualized using PyMOL 2.5.2 with five contour levels of the density map with their respective color: 15σ (red), 10σ (green), 5σ (cyan), 2.5σ (blue), and 1σ (violet). Particles size not drawn to scale of the Dmax. (**K**) particle size distribution of the Moderna mRNA-LNPs based on intensity, volume, and number.

mRNA-LNPs including: (1) a high electron density in the core that likely corresponds to the mRNA-rich region, (2) an adjacent low electron density structure corresponding to the bleb morphology, which could possibly be assigned to mRNA-poor region, (3) an oblong shape, and (4) mRNA seems to been phase separated inside the core as there are two distinct warm-color-coded regions. The overall architecture and bleb morphology, meaning the mRNA-LNP with two distinct regions with contrasting high and low electron density, were also observed by cryo-TEM (Fig. 2G), demonstrating the accuracy of DENSS algorithm. The results also suggested the consistency of the data processing and modeling using the lab-scale SAXS data, as the reconstructed models were consistent across the total lipid concentration range tested (i.e. 3.96 to 19.8 mg/mL).

It is worth noting that the physical diameters of the mRNA-LNPs obtained by cryo-TEM (700–1000 Å) (Fig. 2G) and SAXS (758–852 Å) (Table I) deviate from the hydrodynamic size (1450 Å) because DLS reports z-average number which is intensity based and emphasizes the larger particles of the distribution by $10^6\times$ factor according to the Rayleigh scattering approximation [28]. Number- and volume-based particle sizes are closer to what is detected by cryo-TEM and thus showed mean particle diameter at around 900 Å (Fig. 2H, Figure S2) which closely agrees with the Dmax from SAXS and the cryo-TEM data. Furthermore, the DLS data represents hydrodynamic size which is calculated based on the mobility of the particles using the Stokes–Einstein equation. When the particles diffuse, they drag the surrounding solvents, electrical double layer, which further explains the differences in the particle sizes obtained using three methods.

Finally, when the Moderna's vaccine sample was spiked with external RNAse, there were no significant structural changes observed in the LNPs and the hydrodynamic diameter, mRNA encapsulation efficiency, SAXS profile, Dmax, Rg, and the reconstructed model remained similar (Table II, Fig. 2I-K), indicating that SAXS data and the reconstructed model are accurate representations of the LNPs and the mRNA encapsulated within the LNPs.

Effect of Freeze–Thaw Cycles on mRNA-LNPs as Detected by DENSS

The mRNA-LNPs were subjected to three freeze–thaw cycles by placing the samples in a freezer at -80°C. Physicochemical characterizations demonstrated that the particle size and PDI exhibited a minor increase from 1441 to 1497 Å and from 0.188 to 0.202 respectively (Table III). The mRNA entrapment efficiency exhibited a small decline, from 95.3% to 93.2% (Table III). This decline was associated with a slight decrease in zeta potential from -2.1 to -4.2 mV, possibly due to the leakage of mRNA that then became adsorbed onto the surface of the LNPs. SAXS characterization was also able to detect these subtle changes. The p(r) analysis confirmed a small increase in Dmax from 734 to 750 Å. In addition, the Rg increased from 220 to 244 Å (Table III).

Cryo-TEM images showed that, although the majority of the mRNA-LNP population retained its similarity compared to the pre-freezing state, instances of irregular shapes with several areas of low electron density (resembling background density) adhering to regions of higher density also existed (Fig. 3A-C). This observation suggests the occurrence of fusion between multiple mRNA-LNPs or blank LNPs during the freezing step. This fusion phenomenon can be attributed to cryo-concentration effect, wherein the concentration of LNPs in the unfrozen fraction increases

Table II Pair Distribution Function Analysis of Spikevax® from SAXS Data

Moderna COVID-19 vaccine Degree of concentration	1x	2.5 x	5x	10x	10×RNAsed
I(0)	4.2 ± 0.5	19.7 ± 1.1	35.3 ± 2.9	56.6 ± 4.4	55.5 ± 3.0
Rg (Å)	220 ± 11	264 ± 6	259 ± 9	270 ± 11	255 ± 13
Dmax (Å)	734	776	820	827	825
Total Estimate	0.7225	0.7497	0.6796	0.7824	0.8143
$\chi 2$	1.0541	0.9405	1.1114	0.9253	0.9503

Table III Physicochemical Properties and Pair Distribution Function Analysis of the mRNA-LNPs After Three Freeze–Thaw Cycles

	I(0)	Rg (Å)	Dmax (Å)	χ^2	Size (Å)	PDI	Zeta (mV)	EE (%)
REF	4.2 ± 0.8	220 ± 11	734	1.0541	1441 ± 24	0.188 ± 0.01	-2.1 ± 0.1	95.3 ± 0.3
FT3	6.0 ± 1.2	244 ± 12	750	1.2437	1497 ± 13	0.252 ± 0.023	-4.2 ± 1.2	93.2 ± 0.1

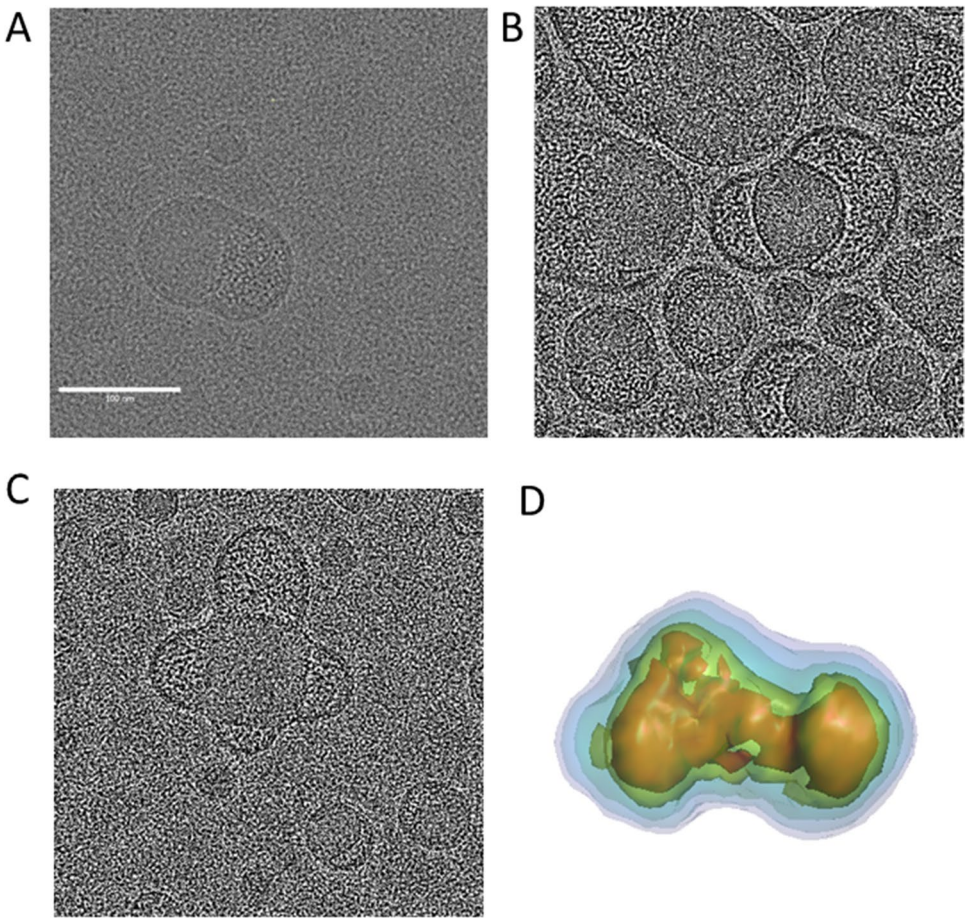

Fig. 3 Moderna COVID-19 vaccine bivalent mRNA-LNPs after three freeze–thaw cycles (**A**) cryo-TEM images and (**B**) reconstructed 3D model by DENSS algorithm.

upon ice formation. In this regard, DENSS failed to reconstruct such a polydispersed particles population (PDI 0.252 compared to the original 0.188) as the reconstructed model did not reconcile between the diverse population of mRNA-LNPs (Fig. 3D *vs* Fig. 1G and Fig. 2D-G).

Effect of RNA on SAXS and DENSS Profiles of LNPs

To study the effect of scattering contrast of the subject (i.e., mRNA-LNPs) and the surrounding environment on the reconstructed models by DENSS, two in-house, one loaded with poly(A) and another not (i.e., 165 and 0 µg/mL, respectively) were synthesized. The SAXS profiles and respective reconstructed models are shown in Fig. 4.

A visual inspection of the SAXS curves for the sample with poly(A) loading reveals signals in the q-value regions extending up to 1250 Å. In contrast, there is limited information in this region for the poly(A)-free sample, likely due to the smaller hydrodynamic size of the poly(A)-free LNPs (1009 Å) compared to the poly(A)-LNP sample (1655 Å) (Table IV). The trend of Dmax, which represents the maximum effective particle dimension and is derived from pair distribution analysis, aligns with the size distribution obtained by DLS (550, 856 Å and 1009, 1665 Å; for poly(A)-free and poly(A)-loaded LNPs, respectively) (Table 4). Both loaded and blank LNPs exhibit a sharp peak, with the d-spacing of the blank LNPs slightly smaller than that of the poly(A)-loaded sample (48 and 54 Å, respectively). The results suggested a multilamellar phase morphology of the LNPs, and further corroborated by the cryo-TEM images (Fig. 4C).

The reconstructed models using the DENSS algorithm of the poly(A)-loaded LNPs (Fig. 4D) demonstrate that LNPs exhibit an ellipsoidal and spherical shape with a high electron density region in the center. In contrast, the reconstructed model of the blank poly(A)-free LNP (Fig. 4E) appears fragmented into many smaller particles, suggesting insufficient contrast between the individual LNP and the surrounding environment. The 'void' observed inside the DENSS image may be attributed to regions in LNP with scattering contrast too low to provide meaningful information and thus reconstruction. Furthermore, the red color coded region indicating high electron density was smaller in blank LNPs compared to poly(A)-loaded LNPs.

Finally, it is noted that a sample mimicking poly(A) leaking by using poly(A)-free LNP with subsequent addition of poly(A) to the LNP suspension was prepared. However, immediately after the addition of poly(A), the sample turned viscous with gel-like properties possibly due to long-chain negatively charged poly(A) acting as

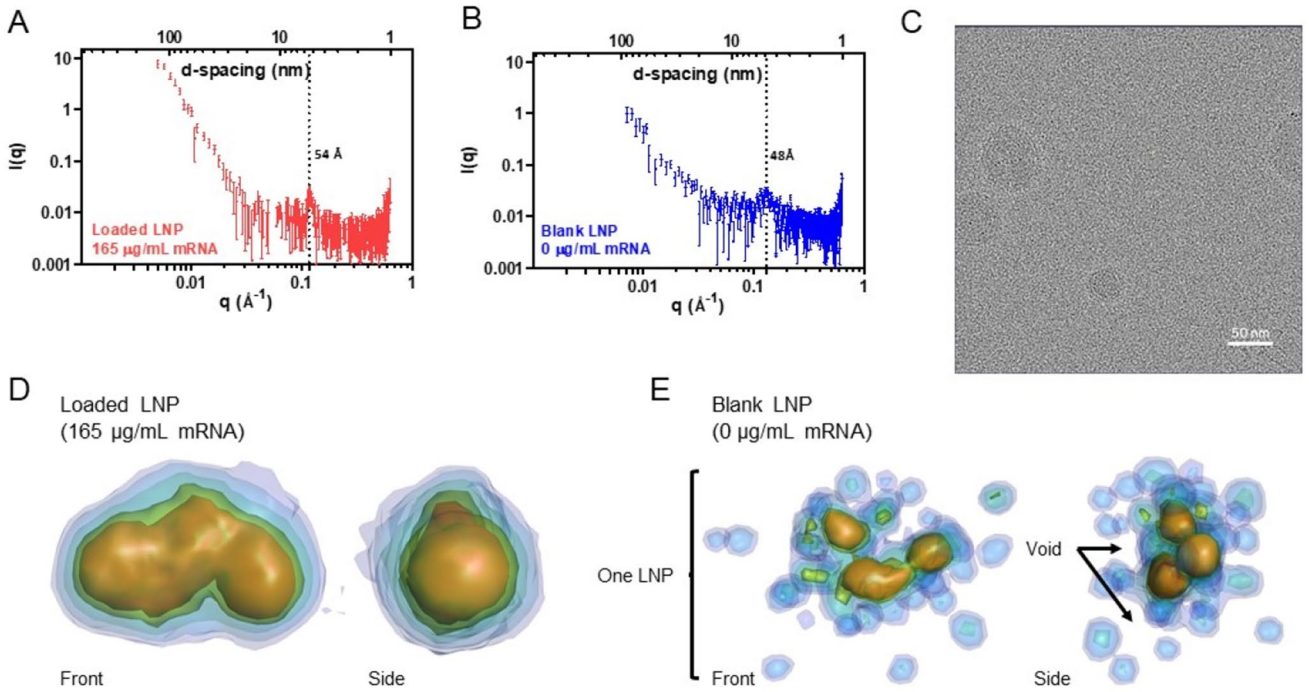

Fig. 4 (**A**-**B**) SAXS profiles of poly(A)-loaded and blank LNPs (165 and 0 µg/mL poly(A), respectively). (**C**) Representative cryo-TEM image of poly(A)-LNPs (reprinted from Int. J. Pharm. with copyright permission) *(24)*. (**D**-**E**) Reconstructed models of loaded and blank poly(A)-LNP.

Table IV Physicochemical Properties and Pair Distribution Function Analysis of the SAXS Profiles of Poly(A)-Loaded and Blank LNPs

mRNA loading	I(0)	Rg (Å)	Dmax (Å)	χ^2	Size (Å)	PDI	EE (%)
Blank (0 µg/mL)	1.2 ± 0.4	184 ± 44	550	1.0609	1009 ± 2	0.121 ± 0.023	N/A
Loaded (165 µg/mL)	12.9 ± 2.3	325 ± 17	856	0.9901	1655 ± 25	0.199 ± 0.001	82.5 ± 3.6

physical crosslinker between the LNPs. Interestingly, the SAXS profile of the resultant sample was different (Figure S3), with two sharp peaks at q values of 0.111 Å and 0.188 Å, indicating the formation of hexagonal structure [29]. Unfortunately and understandably, a DENSS image cannot be reconstructed based on the SAXS profile.

Results of this experiment demonstrated that DENSS is able to differentiate between mRNA loaded and blank LNP based on electron density difference. Furthermore, this experiment further corroborated the reconstructed model of Moderna COVID-19 bivalent vaccine showing bleb structure with two distinct electron density region.

Discussion

The size, shape, and structure of molecules can be examined through the SAXS solution scattering profile, which is frequently employed for protein structure analysis [30, 31]. This is facilitated by algorithms that enable the reconstruction of an envelope delineating the shape of the protein. Although mRNA-LNPs complexes are larger than proteins, they remain within the range of SAXS, with a maximum d-spacing of about 150 nm. This positions SAXS as a suitable method for their physicochemical characterization [32]. SAXS is often viewed as a low-resolution technique (10—100 Å) for proteins, considering their average size, which is less than 100 Å [32]. However, for larger particles, such as mRNA-LNPs, which can reach sizes up to 1500 Å or even larger [33] the resolution offered by SAXS might be sufficient. One major assumption in utilizing ab initio reconstruction from SAXS data of proteins is the assumption of homogenous electron density distribution across the studied systems (e.g., protein, monoclonal antibody). Exceptions exist, particularly for proteins with prosthetic inorganic groups such as metalloproteins with elevated electron density found in the regions with metal ion cofactors [34]. As such, for system known to have different electron density, results obtained from SAXS

is often cross-validated with other techniques like cryo-TEM [35], X-ray crystallography [36], or NMR [37].

In this aspect, the DENSS algorithm differs from dummy atom *ab initio* modeling methods, like DAMMIF [16], by its ability to reconstruct an electron density map using a novel iterative structure factor retrieval algorithm [8, 9]. By differentiating between the mRNA and lipid components, DENSS can potentially provide deeper insights into the structural architecture of mRNA-LNP complexes. For example, commonly used PSD characterizations such as DLS and nanoparticle tracking analysis can only provide information about the hydrodynamic radius, without offering details about the structural information. A case in point are cryo-TEM studies, which have revealed distinctive "bleb" structures containing separate mRNA-loaded and blank segments. These "blebs," which have been widely reported, can form during the dialysis process when blank LNPs merge with mRNA-loaded complexes due to environmental changes [38, 39] Furthermore, it has been shown that mRNA-LNP formulations that use DLin-MC3 as an ionizable lipid predominantly contain two mRNAs per loaded LNP [38], of which most of our reconstruction based on DENSS showed two distinctive high-electron density regions in hotter color (red, green) as opposed to colder color (cyan, blue, violet) (Fig. 2).

It is also worth noting that the absolute electron density and scattering length density difference between RNA and lipids are critical for DENSS to reconstruct a reliable and meaningful model. Specifically, as demonstrated in Fig. 4D-E, the lack of poly(A) leads to uncertainty and thus the existence of void regions in reconstructed model. The lack of high electron density poly(A) in the blank LNP, also resulted in a reduction in red-color regions, an indication of lower probability of finding electrons in that certain 3-dimensional space. Thus, the results from Fig. 4 further corroborate findings from Fig. 2 that the red/green regions in the DENSS reconstructs are likely spatial arrangement of RNA.

The change in Rg due to structural change has been documented as the loading of high electron density drug (DF003) resulted in a reduction of Rg from 17.3 to 15.8; despite an increase in hydrodynamic radius from 30.0 to 36.0 nm [40]. In a similar fashion our study demonstrated a slight increase in Rg when the electron-rich mRNA content leaked outside due to the freeze–thaw stress (Table III, Fig. 3). As a method introduced in 2018, DENSS has encountered its fair share of criticism [41], including (1) inability to differentiate between different contrast, multiple component system such as DNA-wrapped protein, (2) inability to differentiate between identical shapes with sharp density cutoff, and (3) averaging of loosely constrained 3D real-space density leading to artifact of high density region always located in the core [41].

The first criticism directed at DENSS is its inability to distinguish between DNA and proteins within a DNA–protein complex, despite a twofold difference in X-ray contrast. In aqueous solutions, DNA exhibits an X-ray contrast of 0.22 electrons/Å^3, while proteins display 0.10 electrons/Å^3. However, the assumption of a higher density for nucleic acids fails to account for atomic packing. Proteins, often more compact than RNA/DNA which mostly comprise of helical conformation with void spaces between nucleotide strands. This similarity in electron density present a challenge even for cryo-TEM, which inherently has higher resolution than SAXS, in differentiating between the two species [9]. Nonetheless, the X-ray scattering length density which takes into account physical density and intrinsic scattering power of the molecule, for RNA is approximately ~ 16 (10^{10} cm^{-2}) [42], protein ~ 12 (10^{10} cm^{-2}) [42] and phospholipid ~ 6–12 10^{10} cm^{-2} from hydrocarbon chains to phosphate head groups [43]. This disparity leads to distinctions in the DENSS reconstructed models, featuring mRNA-rich high electron density and lipid-rich low electron density regions (Fig. 2), corresponding to the observed bleb structure, also validated by cryo-TEM.

The second criticism pertains to DENSS's inability to differentiate between three identical shapes with sharp density cutoffs [41]. Such electron density profiles are considered unnatural, and these three ellipsoid models yield highly similar scattering profiles, making differentiation a challenging task for any modelling algorithm [9].

The third criticism mentioned the process of averaging multiple loosely constrained 3D real-space densities. This procedure often yields elevated density in the central portion of the final model, regardless of the actual location of high electron density molecules. This criticism has been addressed by artificially doubling the density of DNA within DNA-wrapped histones, thus enhancing the contrast compared to histones. This adjustment results in a final model showcasing a high electron density outer layer and a low-density core [9]. This observation is further substantiated by our data revealing the presence of bleb structures characterized by high and low densities, respectively (Fig. 2).

In general, DENSS is still subject to the same ambiguity and low resolution limiting conventional algorithm, which correspond to a fundamental limitation of SAXS. However, if given sufficient contrast, DENSS is capable of reconstructing multiple density systems. Due to the two times difference in contrast between RNA and lipids, the mRNA-LNP system is a suitable candidate for the reconstruction [42, 43].

With regards to mRNA-LNP research, there is a clear need for additional characterization methods, beyond size, polydispersity index (PDI), and encapsulation efficiency (EE). While cryo-TEM is an important tool, its high cost, narrow scope, and high time-consuming requirement can be a limitation. Conversely, lab-scale SAXS offers simplicity, much wider scope, and shorter run times. These two techniques serve as excellent complements to each

other. Our study has demonstrated that DENSS reconstructions from lab-scale SAXS data are able to resolve the internal structures of the mRNA-LNPs in agreement with cryo-TEM data (Fig. 2D-G). In terms of size, SAXS can accurately estimate the actual size in alignment with cryo-TEM. This is further corroborated by numerous studies that present cryo-TEM images of mRNA-LNPs, demonstrating particle diameters roughly within the 700–1000 Å range [44]. As for shape, SAXS, coupled with DENSS reconstruction, reliably depicts elongated structures. These structures align well with those observed in cryo-TEM studies. When it comes to structure, SAXS can reconstruct the unique "bleb" formations characterized by regions of low electron density (blank sections) and high electron density (sections with 2–3 mRNA copies). These "blebs" form during dialysis due to the re-arrangement and fusion of blank lipid nanoparticles with mRNA-loaded LNPs. Furthermore, SAXS has proven to be a sensitive tool in detecting subtle changes during various treatments and conditions, such as ribonuclease treatment and freeze–thaw cycles.

In summary, SAXS coupled with the DENSS algorithm represents a potent and promising mRNA-LNP characterization method, serving as a quality control checkpoint due to its (a) information richness provided by electron density mapping, (b) minimal sample requirements, and (c) rapid run time. Specifically, a library of reconstructed electron density-mapping models could be collected and subsequently compared to models of samples during storage or downstream processing (e.g., freezing, freeze-drying). Detection of architectural deviations from the original model, not discernible by conventional physicochemical characterization methods (e.g., DLS, fluorescence binding assay), serves as an indicator of problems encountered during such processes.

Conclusions

Pairing SAXS with pair distribution analysis and DENSS algorithm reconstruction enables a more comprehensive view of mRNA-LNPs, encompassing size, shape, and internal structure. The information obtained from the SAXS profile aligns well with data derived from cryo-TEM and DLS. Therefore, SAXS with DENSS algorithm represents a promising method for expansion and incorporation into the standard toolbox of mRNA-LNP physicochemical characterization methods, such as DLS and encapsulation efficiency (EE). This integration could lead to a deeper understanding of mRNA and facilitate future development of products based on mRNA-LNPs.

Supplementary Information The online version contains supplementary material available at https://doi.org/10.1007/s11095-024-03671-9.

Acknowledgements We acknowledge the asistance of Thomas Weiss in performing synchrotron SAXS experiment. Use of the Stanford Synchrotron Radiation Lightsource (SSRL), SLAC National Accelerator Laboratory, is supported by the U.S. Department of Energy (DoE), Office of Science, Office of Basic Energy Sciences under Contract No. DE-AC02-76SF00515. The SSRL Structural Molecular Biology Program is supported by the DOE Office of Biological and Environmental Research, and by the National Institutes of Health, National Institute of General Medical Sciences (P30GM133894). The contents of this publication are solely the responsibility of the authors and do not necessarily represent the official views of NIGMS or DoE.

Author Contributions The manuscript was written with the contributions of all authors. / All authors have approved the final version of the manuscript.

Funding This work was supported by a Sponsored Research Agreement from TFF Pharmaceuticals Inc. (to ROW and ZC).

Data Availability Raw SAXS data were included in the supporting information and also available upon request.

Declarations

Competing Interest ZC and ROW report financial support by TFF Pharmaceuticals, Inc. The terms have been reviewed and approved by UT Austin in accordance with its institutional policy on objectivity in research. ZC reports a relationship with TFF Pharmaceuticals, Inc. that includes equity or stocks and funding grants. ROW reports a relationship with TFF Pharmaceuticals, Inc. that includes consulting or advisory, equity or stocks, and funding grants. ZC, ROW, and KJP have patent(s) and/or patent applications related to thin-film freezing.

References

1. Qin S, Tang X, Chen Y, Chen K, Fan N, Xiao W, *et al*. mRNA-based therapeutics: powerful and versatile tools to combat diseases. Sig Transduct Target Ther. 2022;7(1):166.
2. Oude Blenke E, Örnskov E, Schöneich C, Nilsson GA, Volkin DB, Mastrobattista E, *et al*. The storage and in-use stability of mRNA vaccines and therapeutics: not a cold case. J Pharm Sci. 2023;112(2):386–403.
3. Ai L, Li Y, Zhou L, Yao W, Zhang H, Hu Z, *et al*. Lyophilized mRNA-lipid nanoparticle vaccines with long-term stability and high antigenicity against SARS-CoV-2. Cell Discov. 2023;9(1):9.
4. Zhao P, Hou X, Yan J, Du S, Xue Y, Li W, *et al*. Long-term storage of lipid-like nanoparticles for mRNA delivery. Bioactive Materials. 2020;5(2):358–63.
5. Phyo P, Zhao X, Templeton AC, Xu W, Cheung JK, Su Y. Understanding molecular mechanisms of biologics drug delivery and stability from NMR spectroscopy. Adv Drug Deliv Rev. 2021;174:1–29.
6. Eygeris Y, Patel S, Jozic A, Sahay G. Deconvoluting lipid nanoparticle structure for messenger RNA delivery. Nano Lett. 2020;20(6):4543–9.
7. San Emeterio J, Pollack L. Visualizing a viral genome with contrast variation small angle X-ray scattering. J Biol Chem. 2020;295(47):15923–32.
8. Grant TD. Ab initio electron density determination directly from solution scattering data. Nat Methods. 2018;15(3):191–3.

9. Grant TD. Reply to: Limitations of the iterative electron density reconstruction algorithm from solution scattering data. Nat Methods. 2021;18(3):246–8.
10. Léger C, Pitard I, Sadi M, Carvalho N, Brier S, Mechaly A, *et al*. Dynamics and structural changes of calmodulin upon interaction with the antagonist calmidazolium. BMC Biol. 2022;20(1):176.
11. Doll SG, Meshkin H, Bryer AJ, Li F, Ko YH, Lokareddy RK, *et al*. Recognition of the TDP-43 nuclear localization signal by importin α1/β. Cell Rep. 2022;39(13):111007.
12. Lokareddy RK, Hou CFD, Doll SG, Li F, Gillilan RE, Forti F, *et al*. Terminase subunits from the pseudomonas-phage E217. J Mol Biol. 2022;434(20):167799.
13. Kim M, Kim HS, D'Souza A, Gallagher K, Jeong E, Topolska-Woś A, *et al*. Two interaction surfaces between XPA and RPA organize the preincision complex in nucleotide excision repair. Proc Natl Acad Sci USA. 2022;119(34):e2207408119.
14. Jain M, Golzarroshan B, Lin C, Agrawal S, Tang W, Wu C, *et al*. Dimeric assembly of human Suv3 helicase promotes its RNA unwinding function in mitochondrial RNA degradosome for RNA decay. Protein Science.2022;31:e4312. https://doi.org/10.1002/pro.4312.
15. Liu Y, Munsayac A, Hall I, Keane SC. Solution Structure of NPSL2, A Regulatory Element in the oncomiR-1 RNA. J Mol Biol. 2022;434(18):167688.
16. Franke D, Svergun DI. DAMMIF, a program for rapid ab-initio shape determination in small-angle scattering. J Appl Crystallogr. 2009;42(2):342–6.
17. Guo R, Sumner J, Qian S. Structure of diisobutylene maleic acid copolymer (DIBMA) and its lipid particle as a "Stealth" membrane-mimetic for membrane protein research. ACS Appl Bio Mater. 2021;4(6):4760–8.
18. Fujii S, Sakurai K. Structural analysis of an octameric resorcinarene self-assembly in toluene and its morphological transition by temperature. J Phys Chem Lett. 2021;12(28):6464–8.
19. Takahashi R, Yamamoto K, Sugahara R, Otake R, Hayashi K, Nakamura J, *et al*. In situ and ex situ studies of ring-like assembly of silica nanoparticles in the presence of poly(propylene oxide)–poly(ethylene oxide) block copolymers. Langmuir 2023:39, 32, 11379–387.
20. Sumner J, Qian S. DENSS-multiple: A structure reconstruction method using contrast variation of small-angle neutron scattering based on the DENSS algorithm. BBA Advances. 2022;2:100063.
21. Svergun DI. Restoring low resolution structure of biological macromolecules from solution scattering using simulated annealing. Biophys J. 1999;76(6):2879–86.
22. Patel S, Ashwanikumar N, Robinson E, Xia Y, Mihai C, Griffith JP, *et al*. Naturally-occurring cholesterol analogues in lipid nanoparticles induce polymorphic shape and enhance intracellular delivery of mRNA. Nat Commun. 2020;11(1):983.
23. Schoenmaker L, Witzigmann D, Kulkarni JA, Verbeke R, Kersten G, Jiskoot W, *et al*. mRNA-lipid nanoparticle COVID-19 vaccines: Structure and stability. Int J Pharm. 2021;601:120586.
24. AboulFotouh K, Southard B, Dao HM, Xu H, Moon C, Williams Iii RO, *et al*. Effect of lipid composition on RNA-Lipid Nanoparticle properties and their sensitivity to thin-film freezing and drying. Int J Pharm. 2023;650:123688.
25. Hopkins JB, Gillilan RE, Skou S. ıt BioXTAS RAW: improvements to a free open-source program for small-angle X-ray scattering data reduction and analysis. J Appl Crystallogr. 2017;50(5):1545–53.
26. Svergun DI. Determination of the regularization parameter in indirect-transform methods using perceptual criteria. J Appl Crystallogr. 1992;25(4):495–503.
27. Kremer JR, Mastronarde DN, McIntosh JR. Computer visualization of three-dimensional image data Using IMOD. J Struct Biol. 1996;116(1):71–6.
28. Stetefeld J, McKenna SA, Patel TR. Dynamic light scattering: a practical guide and applications in biomedical sciences. Biophys Rev. 2016;8(4):409–27.
29. Rappolt M, Hickel A, Bringezu F, Lohner K. Mechanism of the lamellar/inverse hexagonal phase transition examined by high resolution x-ray diffraction. Biophys J. 2003;84(5):3111–22.
30. Grant TD, Luft JR, Wolfley JR, Tsuruta H, Martel A, Montelione GT, *et al*. Small angle X-ray scattering as a complementary tool for high-throughput structural studies. Biopolymers. 2011;95(8):517–30.
31. Jeffries CM, Ilavsky J, Martel A, Hinrichs S, Meyer A, Pedersen JS, *et al*. Small-angle X-ray and neutron scattering. Nat Rev Methods Primers. 2021;1(1):70.
32 Kikhney AG, Svergun DI. A practical guide to small angle X-ray scattering (SAXS) of flexible and intrinsically disordered proteins. FEBS Letters. 2015;589(19PartA):2570–7.
33. Di Cola E, Grillo I, Ristori S. Small angle x-ray and neutron scattering: powerful tools for studying the structure of drug-loaded liposomes. Pharmaceutics. 2016;8(2):10.
34. Noodleman L. Mapping elusive electron density. Nat Chem Biol. 2016;12(6):391–2.
35. Callaway E. The protein-imaging technique taking over structural biology. Nature (London). 2020;578(7794):201-201.
36. Smyth MS. x Ray crystallography. Mol Pathol. 2000;53(1):8–14.
37. Hu Y, Cheng K, He L, Zhang X, Jiang B, Jiang L, *et al*. NMR-based methods for protein analysis. Anal Chem. 2021;93(4):1866–79.
38. Li S, Hu Y, Li A, Lin J, Hsieh K, Schneiderman Z, *et al*. Payload distribution and capacity of mRNA lipid nanoparticles. Nat Commun. 2022;13(1):5561.
39. Cheng MHY, Leung J, Zhang Y, Strong C, Basha G, Momeni A, *et al*. Induction of Bleb structures in lipid nanoparticle formulations of mRNA leads to improved transfection potency. Adv Mater. 2023;35(31):2303370.
40. Urimi D, Hellsing M, Mahmoudi N, Söderberg C, Widenbring R, Gedda L, *et al*. Structural characterization study of a lipid nanocapsule formulation intended for drug delivery applications using small-angle scattering techniques. Mol Pharmaceutics. 2022;19(4):1068–77.
41. Konarev PV, Svergun DI. Limitations of the iterative electron density reconstruction algorithm from solution scattering data. Nat Methods. 2021;18(3):244–5.
42. Mahieu E, Gabel F. Biological small-angle neutron scattering: recent results and development. Acta Crystallogr D Struct Biol. 2018;74(8):715–26.
43. Shen C, Woelk C, Kikhney AG, Torres J, Surya W, Harvey RD, *et al*. Absolute scattering length density profile of liposome bilayers obtained by SAXS combined with GIXOS - a tool to determine model biomembrane structure. https://doi.org/10.1101/2022.12.13.520277.
44. Hammel M, Fan Y, Sarode A, Byrnes AE, Zang N, Kou P, *et al*. Correlating the Structure and gene silencing activity of oligonucleotide-loaded lipid nanoparticles using small-angle x-ray scattering. ACS Nano. 2023;17(12):11454–465.